Small-Signal Models With Extended Frequency Range for DC–DC Converters With Large Modulation Ripple Amplitude

Xin Li, Xinbo Ruan, *Fellow, IEEE*, Qian Jin, *Student Member, IEEE*, Mengke Sha, and Chi K. Tse, *Fellow, IEEE*

***Abstract*—Application of pulse width modulation (PWM) is known to produce sideband effects. The accuracy of the models of dc–dc converters can be improved if essential information of the sideband effects of PWM can be incorporated. In this paper, the aliasing effect of the sideband components on the closed-loop control is analyzed, and an effective representation of the transfer function of the pulse-width modulator is derived. Applying this transfer function to the dc–dc converter, an extended-frequency-range small-signal model is obtained, which can be conveniently used for deriving the loop gain of a PWM-controlled dc–dc converter. Furthermore, for wideband control applications, the large switching ripple in the modulation signal necessitates adjustment of the representation of the gain of the pulse-width modulator, which is dependent on the controller. Despite being highly accurate for stability assessment, the extended-frequency-range model is relatively complex after incorporating the effects of the sideband components and the large switching ripple. An approximate approach is introduced to simplify the loop gain expression and to provide physical insights into the effects of the sideband components and large modulation ripple amplitude. Experimental verification of the extended-frequency-range model is provided for a buck converter and a boost converter.**

***Index Terms*—Extended-frequency-range model, large modulation signal, pulse width modulation (PWM), sideband component.**

I. Introduction

PULSE width modulation (PWM) is widely adopted in the control of dc–dc converters. However, the strong nonlinearity of the PWM-controlled dc–dc converters invalidates the direct application of the linear system theory for modeling and analysis of the dynamic performance of such converter systems [1]. The most widely used method for modeling dc–dc converters is the averaging technique [2]–[5], which removes the switching details and permits linear system theory to be used to analyze the characteristics of the converters. However, the validity of the averaged models is subject to the satisfaction of two basic conditions [5]. First, the frequency of the perturbation signal should be much lower than the switching frequency so that the multiple harmonic frequency components and the resulting sideband frequency components can be neglected. Second, the switching ripple amplitude is relatively small, i.e., the ripple amplitudes of the state variables and the modulation signal of the pulse-width modulator are much smaller than their dc respective components. Thus, the bandwidth of the control loop designed using the averaged model is usually limited to one-fifth of the switching frequency. For wide bandwidth applications, the two conditions are not satisfied and the averaged model fails to provide accurate stability information of the closed-loop converter, and the phase margin is usually over-estimated, posing a potential stability issue of the closed-loop system [6].

To improve the accuracy of the models, the multiple harmonic frequency components should be incorporated in modeling, based on which, harmonic balance approaches [7]–[10], and the multiharmonic small-signal modeling method [11], [12] have been proposed. These methods focus on the accurate modeling of the power stage to capture the high-order harmonics of the converters. Besides the power stage, the pulse-width modulator is also nonlinear and will also produce harmonic components [13], [14]. Specifically, upon injecting a small perturbation at frequency ω into the modulation signal, the small-signal response of the output voltage would contain not only the perturbation frequency component, but also sideband components at frequencies $\omega + k\omega_s$ ($k = \pm 1, \pm 2, \ldots$), where ω_s is the angular frequency of the carrier wave. In closed-loop control, the sideband components in the output voltage would cause aliasing effects, which further relegate the accuracy of the averaged model. To improve the accuracy of the model, some attempts have been made to incorporate the aliasing effect of one sideband component at frequency $\omega - \omega_s$, giving a multifrequency small-signal model [15], [16], which is more accurate than the plain-averaged model derived by applying averaging around the switching frequency. Since only ω and $\omega - \omega_s$ components are taken into consideration, the multifrequency small-signal model [15] is also called *two-frequency* model [17]. By incorporating the switching frequency ω_s and another sideband component $\omega + \omega_s$ into the two-frequency model, a new multifrequency

Manuscript received August 15, 2017; revised October 16, 2017; accepted November 9, 2017. Date of publication November 14, 2017; date of current version June 22, 2018. This work was supported by the National Natural Science Foundation of China under Award 51277097. Recommended for publication by Associate Editor R. Redl. *(Corresponding author: Xinbo Ruan.)*

X. Li, X. Ruan, Q. Jin, and M. Sha are with the Center for More-Electric-Aircraft Power System, College of Automation Engineering, Nanjing University of Aeronautics and Astronautics, Nanjing 211106, China (e-mail: lixin_1989@nuaa.edu.cn; ruanxb@nuaa.edu.cn; qian_jin@nuaa.edu.cn; shamengke@nuaa.edu.cn).

C. K. Tse is with the Department of Electronic and Information Engineering, The Hong Kong Polytechnic University, Hong Kong, China (e-mail: michael.tse@polyu.edu.hk).

Color versions of one or more of the figures in this paper are available online at http://ieeexplore.ieee.org.

Digital Object Identifier 10.1109/TPEL.2017.2773641

small-signal model, called the *four-frequency* model, can be obtained [17]. Although the four-frequency model eliminates the phase deviation in low-frequency range that is normally observed in the two-frequency model, it is still inadequate for providing accurate stability information about the converter. In this paper, an extended-frequency-range model, which takes into consideration the effects of all the sideband components, will be proposed to provide accurate stability information. When incorporating all the sideband components, coupling between any two sideband components will occur [18]. For this purpose, a decoupling method is presented in this paper to simplify the model and provide clear physical insight.

In both the basic-averaged model and the two-frequency model, the small ripple is assumed in modeling the pulse-width modulator, and the switching ripple in the modulation signal is neglected. However, the characteristic of the pulse-width modulator varies significantly with the amplitude of the switching ripple [19], [20]. In [17], the impact of the switching ripple on the model was derived by taking only the first-order harmonic component of it into consideration. However, high-order harmonic components also have a significant effect on the model. In this paper, the transfer function of the pulse-width modulator under a large-ripple condition will be investigated by taking all the components into account and an explicit expression will be obtained.

This paper is organized as follows. In Section II, considering all the sideband components, an extended-frequency-range model of the pulse-width modulator is derived, and then an extended-frequency-range small-signal model of the PWM-controlled dc–dc converter is proposed. In Section III, the gain of the pulse-width modulator when the modulation signal has a large-ripple amplitude is derived for improving the accuracy of the model. Since the proposed model results in rather complex transfer functions, an approximation is applied in Section IV to simplify the loop gain expression, allowing convenient physical interpretation of the effects of the sideband components and the large modulation ripple amplitude. Moreover, a simple and practical compensation transfer function design method based on the extended-frequency-range model is proposed for the closed-loop control design. To verify the effectiveness of the proposed model, experimental measurements of a buck converter and a boost converter are presented in Section V. Finally, Section VI concludes this paper.

II. Extended-Frequency-Range Small-Signal Model of PWM DC–DC Converters

A. Extended-Frequency-Range Small-Signal Model of Pulse-Width Modulator

In general, the modulation signal, denoted as $v_{\rm mod}(t)$, is composed of a steady-state part and a small-signal signal

$$v_{\rm mod}(t) = V_{\rm mod}(t) + \hat{v}_{\rm mod}(t) \tag{1}$$

where $V_{\rm mod}(t)$ is the steady-state modulation signal, and $\hat{v}_{\rm mod}(t)$ is the small-signal perturbation signal. Moreover, $V_{\rm mod}(t)$ contains a dc component and a switching ripple component. The small-signal perturbation $\hat{v}_{\rm mod}(t)$ can be expressed as

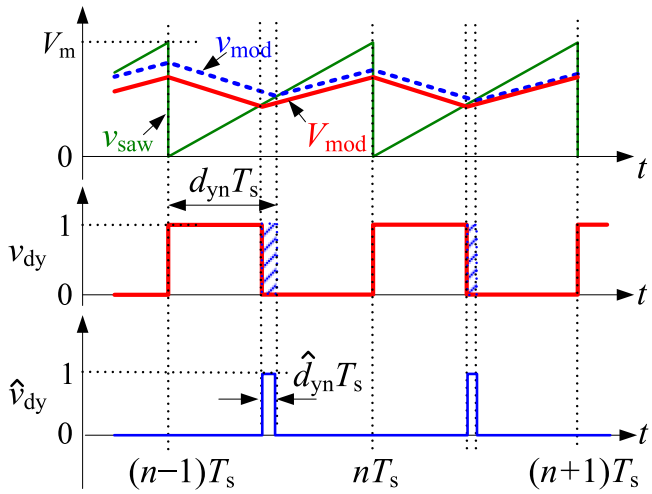

Fig. 1. Key waveforms of the pulse-width modulator with perturbation.

$$\hat{v}_{\rm mod}(t) = \hat{V}_{\rm mod} e^{j(\omega t+\theta)} \tag{2}$$

where $\hat{V}_{\rm mod}$, ω, and θ represent the amplitude, frequency, and initial phase of $\hat{v}_{\rm mod}(t)$, respectively. Fig. 1 shows the key waveforms of a pulse-width modulator, where $v_{\rm saw}$ is the carrier signal with an amplitude of V_m and period of T_s, v_{dy} is the modulator output or the duty-cycle signal, and d_{yn} is the duty cycle at the nth switching period. If the steady-state duty cycle is D_y, and the duty-cycle perturbation at the nth cycle is $\hat{d}_{yn}$, we have

$$d_{yn} = D_y + \hat{d}_{yn}. \tag{3}$$

In each period, the modulation signal is expected to intersect with the carrier signal once, and at the intersecting instant, $v_{\rm mod}$ is equal to $v_{\rm saw}$

$$v_{\rm saw}[(n-1)T_s + d_{yn}T_s] = v_{\rm mod}[(n-1)T_s + d_{yn}T_s] \tag{4}$$

where $(n-1)T_s + d_{yn}T_s$ is the interaction instant in the nth cycle. Substituting (1) and (3) into (4) yields

$$\begin{aligned} &v_{\rm saw}[(n-1)T_s + (D_y + \hat{d}_{yn})T_s] \\ &= V_{\rm mod}[(n-1)T_s + (D_y + \hat{d}_{yn})T_s] \\ &\quad + \hat{v}_{\rm mod}[(n-1)T_s + (D_y + \hat{d}_{yn})T_s]. \end{aligned} \tag{5}$$

By taking the Taylor series expansion of (5) at $(n-1)T_s + D_y T_s$ and ignoring high-order terms, we have

$$\begin{aligned} &v_{\rm saw}[(n-1+D_y)T_s] + \frac{V_m}{T_s}\hat{d}_{yn}T_s \\ &= V_{\rm mod}[(n-1+D_y)T_s] + V'_{\rm mod}(D_yT_s)\hat{d}_{yn}T_s \\ &\quad + \hat{v}_{\rm mod}[(n-1+D_y)T_s] \end{aligned} \tag{6}$$

where $V'_{\rm mod}(D_yT_s)$ is the gradient of $V_{\rm mod}(t)$ at the instant right before $t = (n-1+D_y)T_s$ and $V_{\rm mod}(t)$ can be discontinuous at $t = (n-1+D_y)T_s$.

Eliminating the quiescent values from both sides of (6), the transfer function of the PWM is obtained as

$$\frac{\hat{d}_{yn}}{\hat{v}_{\rm mod}[(n-1+D_y)T_s]} = \frac{1}{V_m - T_s V'_{\rm mod}(D_y T_s)} \triangleq F_m. \quad (7)$$

As shown in Fig. 1, $\hat{v}_{\rm dy}(t)$ is a series of pulses, and the pulse-width in the nth cycle is $\hat{d}_{yn}T_s$. Based on the equal-area principle, $\hat{v}_{dy}(t)$ can be approximated as a string of impulse functions, and the area of $\hat{v}_{dy}(t)$ in the nth cycle is $\hat{d}_{yn}T_s$. Thus, we have

$$\hat{v}_{dy}(t) = \sum_{n=-\infty}^{+\infty} \hat{d}_{yn}T_s\delta[t-(n-1+D_y)T_s] \quad (8)$$

where $\delta(t)$ is the unit impulse function. Then, substituting (7) into (8) gives

$$\hat{v}_{dy}(t) = \sum_{n=-\infty}^{+\infty} F_m \hat{v}_{\rm mod}[(n-1+D_y)T_s]\cdot T_s \cdot \delta[t-(n-1+D_y)T_s]. \quad (9)$$

Since $\delta[t-(n-1+D_y)T_s]$ is zero except at $t=(n-1+D_y)T_s$, (9) can be rewritten as

$$\hat{v}_{dy}(t) = \sum_{n=-\infty}^{+\infty} F_m \hat{v}_{\rm mod}(t)\cdot T_s \cdot \delta[t-(n-1+D_y)T_s] = F_m T_s \hat{v}_{\rm mod}(t)\sum_{n=-\infty}^{+\infty}\delta[t-(n-1+D_y)T_s]. \quad (10)$$

Furthermore, taking the Fourier transform of (10), we obtain [21]

$$\hat{v}_{dy}(t) = F_m T_s \hat{v}_{\rm mod}(t)\sum_{k=-\infty}^{\infty} c_k e^{jk\omega_s t} \quad (11)$$

where $\omega_s = 2\pi/T_s$, and c_k is the Fourier coefficient of the $k\omega_s$ component

$$c_k = \frac{1}{T_s}\int_0^{T_s}\sum_{n=-\infty}^{+\infty}\delta\left(t-nT_s-D_yT_s\right)e^{-jk\omega_s t}dt. \quad (12)$$

During the interval of $[0, T_s]$, we have

$$\sum_{n=-\infty}^{+\infty}\delta\left(t-nT_s-D_yT_s\right) = \delta\left(t-D_yT_s\right). \quad (13)$$

Substituting (13) into (12), c_k can be rewritten as

$$c_k = \frac{1}{T_s}\int_0^{T_s}\delta\left(t-D_yT_s\right)e^{-jk\omega_s t}dt = \frac{1}{T_s}e^{-j2\pi kD_y}\int_0^{T_s}\delta\left(t-D_yT_s\right)dt = \frac{1}{T_s}e^{-j2\pi kD_y}. \quad (14)$$

Putting (2) and (14) into (11) yields

$$\hat{v}_{dy}(t) = F_m\sum_{k=-\infty}^{\infty}\hat{V}_{\rm mod}e^{j[(\omega+k\omega_s)t-2\pi kD_y+\theta]}. \quad (15)$$

From (15), we clearly see that in the presence of sinusoidal modulation disturbance $\hat{v}_{\rm mod}(t)$ at frequency ω, $\hat{v}_{dy}(t)$ has sideband components at frequencies $\omega+k\omega_s$ ($k=\pm1,\pm2,\ldots$).

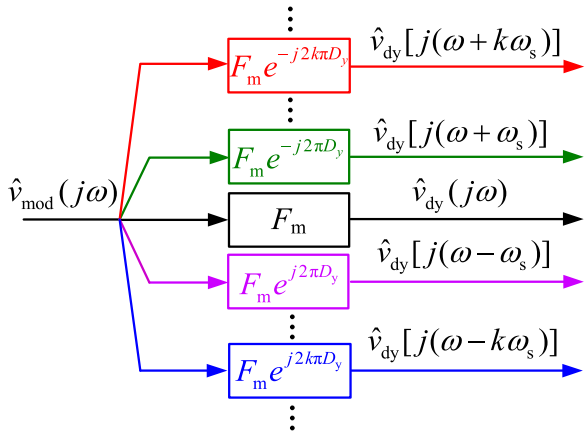

Fig. 2. Extended-frequency-range small-signal model of pulse-width modulator.

This is commonly understood as the sideband effect. Denoting the component at frequency $\omega+k\omega_s$ as $\hat{v}_{dy\_k}(t)$, we can write

$$\hat{v}_{dy\_k}(t) = F_m\hat{V}_{\rm mod}e^{j[(\omega+k\omega_s)t-2\pi kD_y+\theta]} = F_m\hat{v}_{\rm mod}(t)e^{j(k\omega_s t-2\pi kD_y)}. \quad (16)$$

Writing the Fourier coefficients of $\hat{v}_{\rm mod}(t)$ and $\hat{v}_{dy\_k}(t)$ as $\hat{v}_{\rm mod}(j\omega)$ and $\hat{v}_{dy}[j(\omega+k\omega_s)]$, respectively, we have

$$\hat{v}_{\rm mod}(j\omega) = \hat{V}_{\rm mod}e^{j\theta} \quad \text{and}$$

$$\hat{v}_{dy}[j(\omega+k\omega_s)] = F_m\hat{V}_{\rm mod}e^{j(-2\pi kD_y+\theta)}. \quad (17)$$

Then, using (17), the transfer function from $\hat{v}_{\rm mod}(j\omega)$ to $\hat{v}_{\rm dy}[j(\omega+k\omega_s)]$ can be obtained as

$$\frac{\hat{v}_{dy}[j(\omega+k\omega_s)]}{\hat{v}_{\rm mod}(j\omega)} = F_m e^{-j2\pi kD_y}. \quad (18)$$

Thus, the amplitude of $\hat{v}_{dy}[j(\omega+k\omega_s)]$ is amplified by F_m, and the initial phase of $\hat{v}_{dy}[j(\omega+k\omega_s)]$ lags $\hat{v}_{\rm mod}(j\omega)$ by an angle of $2\pi kD_y$. Based on this, the extended-frequency-range small-signal model of PWM can be represented by the block diagram shown in Fig. 2.

B. Aliasing Effect of PWM

As mentioned above, $\hat{v}_{dy}(t)$ contains both the perturbation-frequency component and the sideband components, and the generated output voltage $\hat{v}_{\rm o}(t)$, thus, contains sideband components in addition to the perturbation-frequency component. In closed-loop control, all frequency components in $\hat{v}_{\rm o}(t)$ are fed back to the pulse-width modulator, contributing to additional perturbation-frequency and sideband components in $\hat{v}_{\rm mod}(t)$. When taking all the sideband components into account, the spectral width of $\hat{v}_{\rm mod}(t)$ is much higher than Nyquist frequency ($\omega_s/2$). According to Shannon sampling theorem, after $\hat{v}_{\rm mod}(t)$ being sampled by the PWM modulator, the spectra of the duty cycle produced by the high-frequency components ($>\omega_s/2$) and the low-frequency component ($<\omega_s/2$) in $\hat{v}_{\rm mod}(t)$ will overlap. This is the aliasing effect of PWM modulator. Similar to (18), the transfer function from any frequency component in

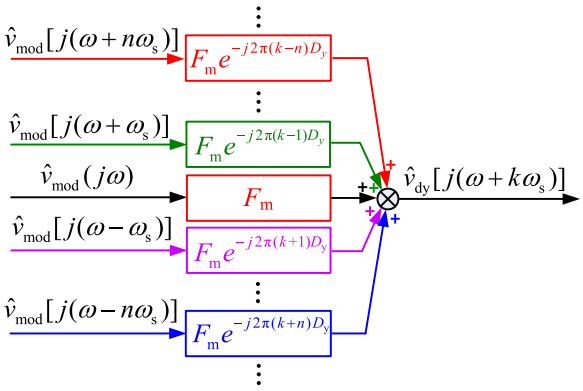

Fig. 3. Generation of $\hat{v}_{dy}[j(\omega+k\omega_s)]$ via feedback.

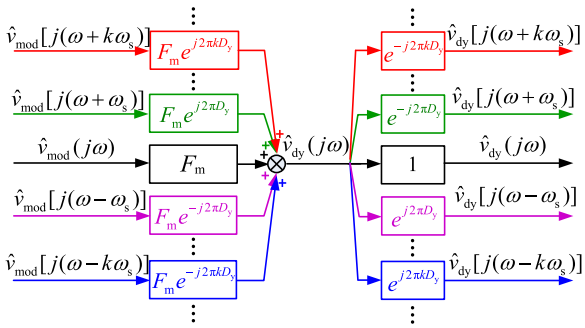

Fig. 4. Control block diagram of PWM incorporating the aliasing effect.

the modulation signal to any frequency component in the duty cycle can be obtained as

$$\frac{\hat{v}_{dy}[j(\omega+k\omega_s)]}{\hat{v}_{\rm mod}[j(\omega+n\omega_s)]} = F_m e^{-j2\pi(k-n)D_y} \quad (n=\pm1,\pm2,\ldots;k=\pm1,\pm2,\ldots). \tag{19}$$

According to (19), the combined effect of the perturbation-frequency component and sideband components on $\hat{v}_{dy}[j(\omega+k\omega_s)]$ can be illustrated by the block diagram shown in Fig. 3. Direct inspection of Fig. 3 gives the expression of $\hat{v}_{dy}[j(\omega+k\omega_s)]$ as

$$\begin{aligned}\hat{v}_{dy}[j(\omega+k\omega_s)] &= \sum_{n=-\infty}^{\infty} \hat{v}_{\rm mod}\,[j(\omega+n\omega_s)]F_m e^{-j2\pi(k-n)D_y} \\ &= e^{-j2\pi kD_y}\sum_{n=-\infty}^{\infty}\hat{v}_{\rm mod}[j(\omega+n\omega_s)]F_m e^{j2\pi nD_y}.\end{aligned} \tag{20}$$

As a special case, when $k=0$, $\hat{v}_{dy}(j\omega)$ is

$$\hat{v}_{dy}(j\omega) = \sum_{n=-\infty}^{\infty}\hat{v}_{\rm mod}[j(\omega+n\omega_s)F_m e^{j2\pi nD_y}. \tag{21}$$

Comparing (20) with (21), we see that $\hat{v}_{dy}[j(\omega+k\omega_s)]$ has the same magnitude as $\hat{v}_{dy}(j\omega)$ but an initial phase lag of $2\pi kD_y$

$$\hat{v}_{dy}[j(\omega+k\omega_s)] = \hat{v}_{dy}(j\omega)e^{-j2\pi kD_y}. \tag{22}$$

From Fig. 3 and (22), the final control block diagram of the pulse-width modulator is given in Fig. 4, where the aliasing effect of all the sideband frequencies is included to provide a fuller and more accurate description of the characteristic of PWM.

C. Extended-Frequency-Range Small-Signal Model of DC–DC Converters

Using the block diagram of Fig. 4, the extended-frequency-range small-signal model of the closed-loop dc–dc converter can be represented as shown in Fig. 5, where H_v is the output voltage sense gain, $G_{vd}(j\omega)$ is the duty-cycle-to-output -voltage transfer function (the general expression can be found in [22]), and $G_v(j\omega)$ is the compensation transfer function. Obviously, each frequency component forms an independent loop of its own at the node of $\hat{v}_{dy}(j\omega)$.

From Fig. 5, the transfer function from $\hat{v}_{\rm mod}(j\omega)$ to $\hat{v}_{dy}(j\omega)$ is obtained as

$$G_{\rm PWM}(j\omega) = \frac{\hat{v}_{dy}(j\omega)}{\hat{v}_{\rm mod}(j\omega)} = \frac{F_m}{1+\sum_{\substack{k=-\infty\\k\neq0}}^{+\infty}T_0[j(\omega+k\omega_s)]} \tag{23}$$

where $T_0[j(\omega+k\omega_s)]=G_v[j(\omega+k\omega_s)]F_m G_{vd}[j(\omega+k\omega_s)]H_v$ represents the loop gain of the sideband component at $\omega+k\omega_s$. Obviously, $G_{\rm PWM}(j\omega)$ is no longer constant, but is related to $T_0[j(\omega+k\omega_s)]$.

Using (23), the block diagram of Fig. 5 can be simplified to Fig. 6, and the complete loop gain expression is given as

$$T(j\omega) = \frac{T_0(j\omega)}{1+\sum_{\substack{k=-\infty\\k\neq0}}^{+\infty}T_0[j(\omega+k\omega_s)]}. \tag{24}$$

As a special case, if only the sideband component at $\omega-\omega_s$ is considered, i.e., $k=-1$, the expression of the loop gain is identical to the two-frequency model in [15]

$$T_{\rm multi\_2}(j\omega) = \frac{T_0(j\omega)}{1+T_0[j(\omega-\omega_s)]}. \tag{25}$$

If only the sideband component at $\omega-\omega_s$ and $\omega+\omega_s$ is considered, i.e., $k=\pm1$, the expression of the loop gain is identical to the four-frequency model in [17]

$$T_{\rm multi\_4}(j\omega) = \frac{T_0(j\omega)}{1+T_0[j(\omega-\omega_s)]+T_0[j(\omega+\omega_s)]}. \tag{26}$$

III. Derivation of Modulator Gain Under Large-Ripple Condition

As pointed out in Section II, the modulator gain F_m is related to the gradient of the modulation signal $V'_{\rm mod}(D_yT_s)$, as given in (7). Under the small-ripple assumption, we have $V'_{\rm mod}(D_yT_s)\approx0$, giving $F_m\approx1/V_m$, which is consistent with the averaged model. However, for applications requiring a wide control bandwidth, the small-ripple assumption is no longer valid. In fact, when the modulator ripple $V'_{\rm mod}(t)$ is relatively large, referred to as the large-ripple condition, the expression of F_m should be revised.

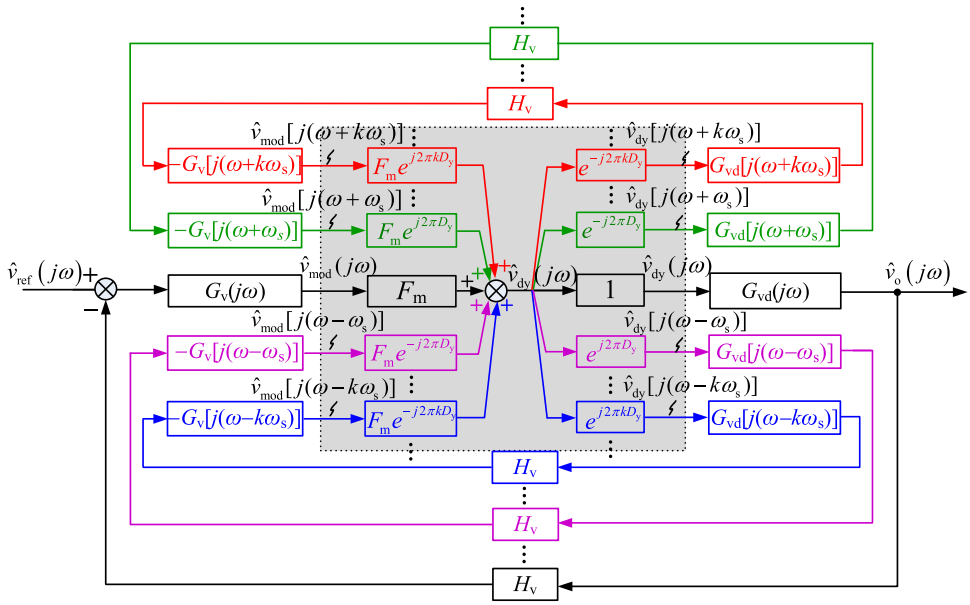

Fig. 5. Control block diagram of the extended-frequency-range model of dc–dc converter.

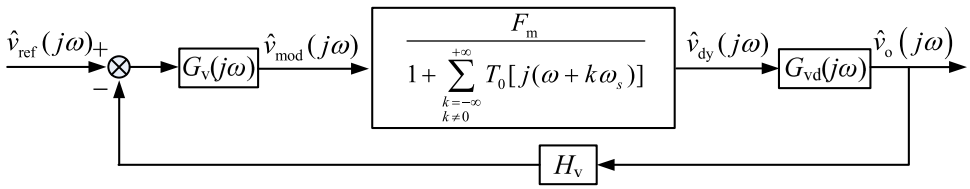

Fig. 6. Simplified control block diagram of the extended-frequency-range small-signal model of closed-loop dc–dc converter.

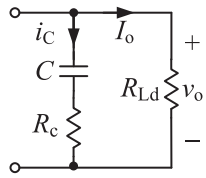

Fig. 7. Schematic diagram of the converter output terminal for basic converters.

Fig. 7 shows the output circuit of any basic dc–dc converter, in which, C is the output filter capacitor, R_c is the equivalent series resistor (ESR) of the output filter, and R_{Ld} is the load resistor. In the steady state, the output voltage ripple ΔV_o is expressed as

$$\Delta V_o(s) = I_C(s)\left(\frac{1}{sC} + R_c\right) \tag{27}$$

where $I_c(s)$ is the capacitor current expression in the s domain.

According to the block diagram of Fig. 6, the switching ripple of the modulation signal can be written as

$$\begin{aligned}\Delta V_{mod}(s) &= -\Delta V_o(s) H_v G_v(s) \\ &= -I_C(s)\left(\frac{1}{sC} + R_c\right) H_v G_v(s). \end{aligned} \tag{28}$$

Upon differentiating the modulation signal, we have

$$\begin{aligned}V'_{mod}(s) &= \Delta V'_{mod}(s) \\ &= s\Delta V_{mod}(s) \\ &= -I_C(s)\left(\frac{1}{C} + sR_c\right) H_v G_v(s). \end{aligned} \tag{29}$$

Obviously, since $V'_{mod}(s)$ is closely related to the compensation transfer function $G_v(s)$, so is F_m. Here, the buck converter with proportional-integral (PI) feedback control is taken as an example to illustrate the derivation of F_m under large-ripple condition. The transfer function of the PI controller can be expressed as

$$G_v(s) = K_p + \frac{K_i}{s} \tag{30}$$

where K_p and K_i are the proportional and integral gains, respectively.

To achieve an adequate phase margin, the corner frequency of $G_v(j\omega)$, denoted as $f_L = K_i/(2\pi K_p)$, should be far below the cutoff frequency f_c of the system. Thus, for frequencies above the switching frequency, (30) can be approximated to

$$G_v(s) = K_p. \tag{31}$$

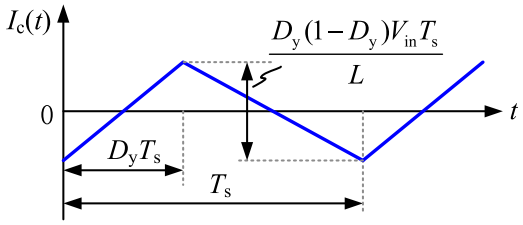

Fig. 8. Waveform of the output capacitor current of the buck converter.

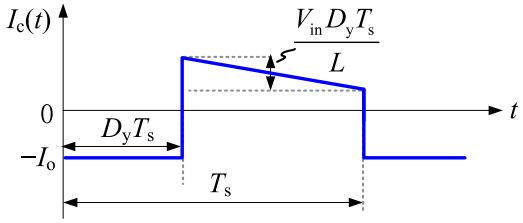

Fig. 9. Waveform of the output capacitor current of the boost and buck–boost converters.

Substituting (31) into (29) leads to

$$V'_{\text{mod}}(s) = -I_C(s)\left(\frac{1}{C} + sR_c\right)H_vK_p. \tag{32}$$

Taking the inverse Laplace transformation of (32), we have

$$V'_{\text{mod}}(t) = -K_pH_v\left[R_cI'_C(t) + \frac{I_C(t)}{C}\right]. \tag{33}$$

Letting $t = D_yT_s$, $V'_{\text{mod}}(D_yT_s)$ is calculated as

$$V'_{\text{mod}}(D_yT_s) = -K_pH_v\left[R_cI'_C(D_yT_s) + \frac{I_C(D_yT_s)}{C}\right]. \tag{34}$$

For the buck converter, Fig. 8 shows the steady-state waveform of the output capacitor current ripple $I_{C\_\text{bu}}(t)$. As seen, $I_{C\_\text{bu}}(t)$ within $(0, D_yT_s]$ can be expressed as

$$I_{C\_\text{bu}}(t) = \frac{(1-D_y)V_{in}}{L}t - \frac{D_y(1-D_y)V_{in}T_s}{2L}. \tag{35}$$

Substituting (35) into (34) yields

$$V'_{\text{mod\_bu}}(D_yT_s) = -\frac{(1-D_y)K_pH_vV_{in}}{LC}(R_cC + 0.5D_yT_s). \tag{36}$$

Putting (36) into (7), the expression of F_m for the buck converter is obtained as

$$F_{m\_\text{bu}} = \frac{1}{V_m + \frac{(1-D_y)K_pH_vV_{in}T_s}{LC}(R_cC + 0.5D_yT_s)}. \tag{37}$$

For the boost and buck–boost converters, the steady-state waveforms of the output capacitor currents are the same, as depicted in Fig. 9, from which the expressions of $I_{C\_\text{bst}}(t)$ and $I_{C\_\text{bb}}(t)$ within $(0, D_yT_s)$ are obtained as

$$I_{C\_\text{bst}}(t) = -I_o = -\frac{V_{in}}{(1-D_y)R_{Ld}} \tag{38}$$

$$I_{C\_\text{bb}}(t) = -I_o = -\frac{D_yV_{in}}{(1-D_y)R_{Ld}}. \tag{39}$$

Substituting (38) and (39) into (34), the expressions of $V'_{\text{mod}}(D_yT_s)$ for the boost and buck–boost converters can be obtained. Putting them into (7), and F_{m_bst} and F_{m_bb} are finally derived as

$$F_{m\_\text{bst}} = \frac{1}{V_m + \frac{K_pH_vV_{in}T_s}{(1-D_y)R_{Ld}C}} \tag{40}$$

$$F_{m\_\text{bb}} = \frac{1}{V_m + \frac{D_yK_pH_vV_{in}T_s}{(1-D_y)R_{Ld}C}}. \tag{41}$$

IV. Effect of Controller on the Extended-Frequency-Range Small-Signal Model

As seen in (24), the complete loop gain contains an infinite series which is dependent on the controller, making it rather inconvenient to apply in practical control design. Here, we propose to use an approximate expression of the loop gain. A buck converter with PI control will be used as an example to illustrate the approximation.

A. Approximation of the Extended-Frequency-Range Model

Comparing (23) with (24), the infinite series in $T(j\omega)$ is originated from $G_{\text{PWM}}(j\omega)$. Thus, we first find an approximation for $G_{\text{PWM}}(j\omega)$. Since the corner frequency of $G_v(j\omega)$ is far below than the cutoff frequency, $G_v(j\omega)$ can be approximated as a proportional gain at the sideband frequencies. Hence, (23) is rewritten as

$$G_{\text{PWM}}(j\omega) = \frac{F_m}{1 + \sum_{\substack{k=-\infty \\ k\neq 0}}^{+\infty} H_vF_mG_{vd}[j(\omega + k\omega_s)]K_p}. \tag{42}$$

The infinite series in (42) can thus be expressed as [21]

$$\begin{aligned}\sum_{\substack{k=-\infty \\ k\neq 0}}^{+\infty} & H_vF_mG_{vd}[j(\omega + k\omega_s)]K_p \\ &= H_vF_mK_p\left(\sum_{k=-\infty}^{+\infty} G_{vd}[j(\omega + k\omega_s)] - G_{vd}(j\omega)\right) \\ &= H_vF_mK_pT_s\left[G^*_{vd}(j\omega) - G_{vd}(j\omega)\right]\end{aligned} \tag{43}$$

where $G^*_{vd}(j\omega)$ represents the sampled function of $G_{vd}(j\omega)$, which has a standard form given by Middlebrook [2]

$$G_{vd}(j\omega) = \frac{V_{in}(1 + j\omega R_cC)}{(j\omega)^2LC + j\omega\left(\frac{L}{R_{Ld}} + R_cC\right) + 1} \tag{44}$$

for the buck converter. Upon sampling $G_{vd}(j\omega)$ and rearranging, we have [21]

$$G^*_{vd}(j\omega) = \frac{V_{in}R_c}{L}\frac{1}{a-b}\left(\frac{a-2c}{e^{(j\omega+0.5a)T_s}-1} + \frac{2c-b}{e^{(j\omega+0.5b)T_s}-1}\right) \tag{45}$$

where

$$a = \frac{R_c}{L} + \frac{1}{R_{Ld}C} + \sqrt{\left(\frac{R_c}{L} + \frac{1}{R_{Ld}C}\right)^2 - \frac{4}{LC}} \tag{46a}$$

$$b = \frac{R_c}{L} + \frac{1}{R_{Ld}C} - \sqrt{\left(\frac{R_c}{L} + \frac{1}{R_{Ld}C}\right)^2 - \frac{4}{LC}} \tag{46b}$$

$$c = \frac{1}{R_c C}. \tag{46c}$$

Although the result in (45) is accurate, the existence of $e^{(j\omega+0.5a)Ts}$ and $e^{(j\omega+0.5b)Ts}$ in (45) makes it hard to appreciate the physical meaning of the proposed model. For this purpose, an approximation should be made on (45).

In practice, the output voltage ripple of the dc–dc converters can be effectively attenuated by a low-pass filter inserted in the power stage. Thus, the following relationships are satisfied:

$$R_{Ld}C >> T_s/(2\pi),\ L/R_c >> T_s/(2\pi),\ LC >> T_s^2/(4\pi^2). \tag{47}$$

Therefore

$$aT_s << 1,\quad bT_s << 1. \tag{48}$$

Using (48) and applying Padé transformation on (45) [23], [24], we have

$$e^{(j\omega+0.5a)T_s} \approx \frac{1 + 0.5(j\omega + 0.5a)T_s + \left[\frac{(j\omega+0.5a)T_s}{\pi}\right]^2}{1 - 0.5(j\omega + 0.5a)T_s + \left[\frac{(j\omega+0.5a)T_s}{\pi}\right]^2} \tag{49a}$$

$$e^{(j\omega+0.5b)T_s} \approx \frac{1 + 0.5(j\omega + 0.5b)T_s + \left[\frac{(j\omega+0.5b)T_s}{\pi}\right]^2}{1 - 0.5(j\omega + 0.5b)T_s + \left[\frac{(j\omega+0.5b)T_s}{\pi}\right]^2}. \tag{49b}$$

The above approximation holds true below half of the switching frequency.

Putting (46) and (49) into (45) and upon rearrangement, we have

$$G_{vd}^*(j\omega) = \frac{1}{T_s}G_{vd}(j\omega) + V_{in}\frac{R_c}{L}\left[\frac{T_s}{\pi^2}\left(j\omega + \frac{R_c}{L} + \frac{1}{R_{Ld}C} - \frac{1}{R_c C}\right) - 0.5\right]. \tag{50}$$

Substitution of (50) into (43), we obtain

$$\sum_{\substack{k=-\infty \\ k\neq 0}}^{+\infty} H_v F_m G_{vd}[j(\omega + k\omega_s)]K_p = H_v F_m K_p T_s V_{in}\frac{R_c}{L}\left[\frac{T_s}{\pi^2}\left(j\omega + \frac{R_c}{L} + \frac{1}{R_{Ld}C} - \frac{1}{R_c C}\right) - 0.5\right]. \tag{51}$$

Using (47), (50) can be approximated as

$$\sum_{\substack{k=-\infty \\ k\neq 0}}^{+\infty} H_v F_m G_{vd}[j(\omega + k\omega_s)]K_p = H_v F_m K_p T_s V_{in}\frac{R_c}{L}\left[\frac{T_s}{\pi^2}\left(j\omega - \frac{1}{R_c C}\right) - 0.5\right]. \tag{52}$$

Substituting (52) and (37) into (42), a simplified expression for $G_{\mathrm{PWM}}(j\omega)$ is derived as

$$G_{\mathrm{PWM}}(j\omega) = \frac{1}{V_m + \frac{H_v K_p T_s V_{in}}{LC}\left[j\omega R_c C\frac{T_s}{\pi^2} + R_c C(0.5 - D_y) + \left(\frac{D_y(1-D_y)}{2} - \frac{1}{\pi^2}\right)T_s\right]}. \tag{53}$$

Putting (53) into (24), a simplified loop gain expression is finally obtained as

$$T(j\omega) = \frac{H_v G_{vd}(j\omega)\left(K_p + \frac{K_i}{j\omega}\right)}{V_m + \frac{H_v K_p T_s V_{in}}{LC}\left[j\omega R_c C\frac{T_s}{\pi^2} + R_c C(0.5 - D_y) + \left(\frac{D_y(1-D_y)}{2} - \frac{1}{\pi^2}\right)T_s\right]}. \tag{54}$$

B. Controller Design Method

The loop gain after compensation is not equal to the product of the compensation transfer function and the uncompensated loop gain, as clearly shown in (54). This differs from the usual control loop design based on the averaged model. Thus, a new control design method has to be developed for the extended-frequency-range model.

Suppose f_c is the cutoff frequency and PM is the phase margin of the system. Then, we may write

$$T(j2\pi f_c) = -\cos(\mathrm{PM}) - j\sin(\mathrm{PM}). \tag{55}$$

According to (54), the expression of the loop gain at cutoff frequency $T(j2\pi f_c)$ can be represented as

$$T(j2\pi f_c) = \frac{K_p M + \frac{K_i}{j2\pi f_c}M}{V_m + K_p N} \tag{56}$$

where

$$M = H_v G_{vd}(j2\pi f_c) \tag{57a}$$

$$N = \frac{H_v T_s V_{in}}{LC}\cdot\left[j\omega R_c C\frac{T_s}{\pi^2} + R_c C(0.5 - D_y) + \left(\frac{D_y(1-D_y)}{2} - \frac{1}{\pi^2}\right)T_s\right]. \tag{57b}$$

TABLE I
PARAMETERS OF THE BUCK CONVERTER

Parameter	Symbol	Value	Parameter	Symbol	Value
Input votlage	V_{in}	80 V	Output capacitor	C	240 μF
Output voltage	V_o	54 V	Capacitor ESR	R_c	0.14 Ω
Output power	P_o	500 W	Peak to peak value	V_m	1.75 V
Switching frequency	f_s	100 kHz	Voltage feedback factor	H_v	0.05
Inductor	L	95 μH			

From (55) and (56), we obtain K_p and K_i as

$$K_p = V_m \frac{-\cos(\mathrm{PM} - \arg M)}{|M| + |N|\cos(\mathrm{PM})\cos(\mathrm{PM} - \arg M + \arg N)} \tag{58}$$

$$K_i = 2\pi f_c V_m \frac{|M|\sin(\mathrm{PM} - \arg M) - |N|\sin(\arg N)}{|M|^2 + |MN|\cos(\mathrm{PM})\cos(\mathrm{PM} - \arg M + \arg N)}. \tag{59}$$

where $|.|$ and arg(.) represent the amplitude and angle of a complex number, respectively.

Taking the buck converter as an example, the main circuit parameters are given in Table I. Here, two controllers with a low ($f_{c1} = 10$ kHz) and a high ($f_{c2} = 40$ kHz) cutoff frequency, respectively, are taken as examples to validate the controller design method. Setting PM = 45°, and putting it to (58) and (59), the controllers are calculated as

$$G_{v\_\mathrm{bu1}}(j\omega) = 15 + \frac{330000}{j\omega} \tag{60}$$

$$G_{v\_\mathrm{bu2}}(j\omega) = 62 + \frac{700000}{j\omega}. \tag{61}$$

The Bode diagrams of the loop gain of the extended-frequency-range model before and after approximation as well as the simulated responses by simulation tool to verify the proposed model are given in Fig. 10. Here, we observe that both controllers meet the design targets and the proposed model produces response curves closely resembling the simulated response curves. Besides, from Fig. 10, the approximation model exhibits good consistency with the accurate one up to half of the switching frequency, proving the validity of the approximation.

C. Effect of Controller on Loop Gain

In the averaged model, the transfer function of the pulse-width modulator is a constant and is expressed as

$$G_{\mathrm{PWM\_av}}(j\omega) = 1/V_m \tag{62}$$

where V_m is the magnitude of the triangular carrier signal.

Comparing (53) and (62), it can be found that the sideband components and the large switching ripple of the modulation

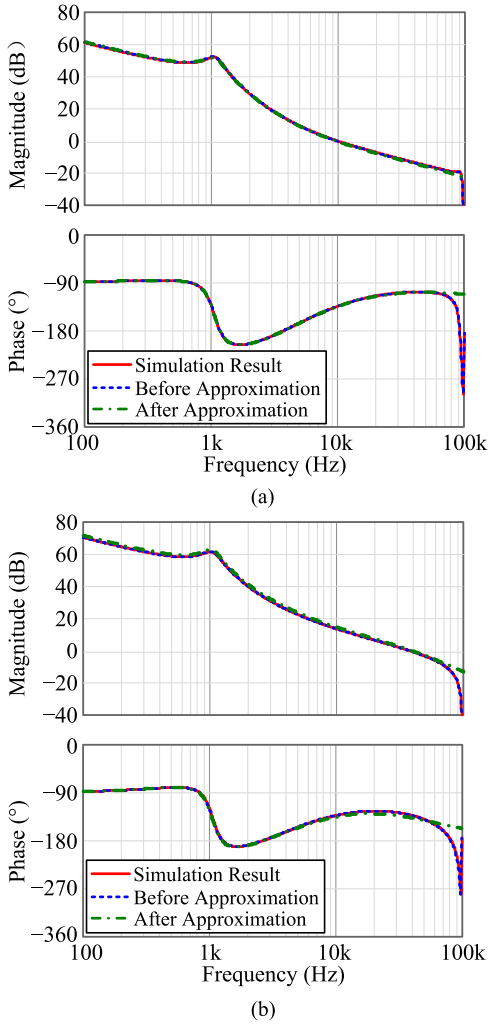

Fig. 10. Bode diagrams of loop gains from the extended-frequency-range model of the buck converter and the simulated results with (a) $G_{v\_\mathrm{bu1}}(s)$ and (b) $G_{v\_\mathrm{bu2}}(s)$ as the controller.

signal on $G_{\mathrm{PWM}}(j\omega)$ effectively introduce a first-order low-pass filter to the loop. Therefore, (53) can be rewritten as

$$G_{\mathrm{PWM}}(j\omega) = \frac{1}{(V_m + K_f)\left(1 + \dfrac{j\omega}{\omega_{L\_\mathrm{PWM}}}\right)} \tag{63}$$

where

$$\omega_{L\_\mathrm{PWM}} = \pi^2 \cdot \frac{V_m LC + V_{in} H_v T_s^2 K_p \left[\frac{R_c C}{T_s}(0.5 - D_y) + \frac{D_y(1-D_y)}{2} - \frac{1}{\pi^2}\right]}{R_c C V_{in} H_v T_s^2 K_p} \tag{64a}$$

$$K_f = \frac{V_{in} H_v T_s^2}{LC} K_p \left[\frac{R_c C}{T_s}(0.5 - D_y) + \left(\frac{D_y(1-D_y)}{2} - \frac{1}{\pi^2}\right)\right]. \tag{64b}$$

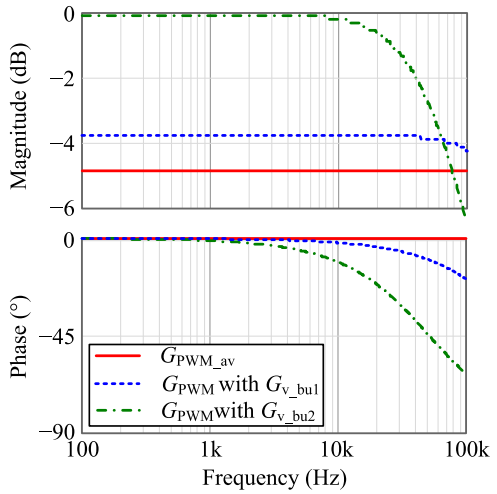

Fig. 11. Bode diagrams of the PWM transfer function with different controllers.

Moreover, for the low-frequency range, i.e., frequencies much lower than the corner frequency ω_{L_PWM}, $G_{PWM}(j\omega)$ is a constant and is expressed as

$$G_{PWM}(j\omega) = 1/\left(V_m + K_f\right). \tag{65}$$

According to (65), when $K_f > 0$, the PWM gain is smaller than $1/V_m$; otherwise, it is larger than $1/V_m$. Besides, when ω increases, the magnitude of $G_{PWM}(j\omega)$ decreases and the phase of it lags due to the equivalent first-order low-pass filter. This rule differs from the one in the averaged model. According to (64), K_f is proportional to K_p, and ω_{L_PWM} decreases with the increasing value of K_p. As the control loop bandwidth gets wider, the value of K_p should be larger. Therefore, as the bandwidth gets wider, the value of K_f is larger and the value of ω_{L_PWM} becomes smaller, and eventually the resultant phase lag will be larger. Thus, we may conclude that for wide loop bandwidth applications, the sideband components and the switching ripple of the modulation signal are not well attenuated, and consequently, the first-order low-pass filter effect will dominate in the loop.

For the purpose of illustration, Fig. 11 shows the Bode diagrams of $G_{PWM}(j\omega)$ with compensation transfer functions $G_{v\_bu1}(j\omega)$ and $G_{v\_bu2}(j\omega)$. Here, we observe that when the cutoff frequency is low, G_{PWM_av} resembles G_{PWM}, revealing that the loop gain derived from the averaged model is basically the same as the extended-frequency-range model for low-frequency applications, as illustrated in Fig. 12(a). In contrast, when the cutoff frequency is high, G_{PWM_av} differs significantly from G_{PWM} and predicts a larger phase shift in the high-frequency range compared to G_{PWM}. Hence, the averaged model tends to over-estimate the phase margin, as shown in Fig. 12(b), and hence offers inaccurate stability information.

D. Comparison With Two-Frequency Model and Four-Frequency Model

Comparing the loop gain expressions (24)–(26), it is obviously that the two-frequency model and the four-frequency model are special cases of the extended-frequency-range model. The condition that the two-frequency model and the four-frequency model hold is that the higher frequency components, i.e., $n\omega_s$, $\omega \pm n\omega_s$ ($n \geq 2$), can be well attenuated. However, in wide bandwidth occasions, this condition is not always satisfied. Taking the aforementioned buck converter with G_{v_bu2} as an example, Fig. 13 shows the spectra of the sideband components in v_{dy}, v_{mod} and v_o after imposing1mV, 40 kHz sinusoidal perturbation into v_{mod}. As seen in Fig. 13, all the sideband components in v_{dy} share the same magnitude, the sideband components in v_{mod} and v_o decrease as the frequency increases. The magnitude of the $\omega - 2\omega_s$ (160 kHz) component in v_{mod} is nearly the same as that of $\omega + \omega_s$ (140 kHz), hence cannot be neglected. For other higher sideband components, though each of their magnitudes is relevantly small, their combined action still cannot be ignored because of the infinity in numbers.

Besides, the expressions of F_m for the two-frequency model and the four-frequency model also differ from our proposed model. In the two-frequency model, the slope of V_{mod} is omitted, while in the four-frequency model, the slope of V_{mod} is approximated obtained by considering only the ω_s component in V_{mod}, namely, $V_{\text{mod\_0}}$. There is a deviation between V_{mod} and $V_{\text{mod\_0}}$ in wide bandwidth occasions. Fig. 14 gives the waveforms of V_{mod} and $V_{\text{mod\_0}}$ of the buck converter with G_{v_bu2}. From Fig. 14, the slope of V_{mod} and $V_{\text{mod\_0}}$ at the interaction instant is 8.9×10^4 V/s and -1.25×10^5 V/s, respectively. Therefore, the calculated F_m by V_{mod} and $V_{\text{mod\_0}}$ are 1.12 and 0.33, respectively, which introduces 10.6 dB deviation. Thus, the $n\omega_s$ ($n \geq 2$) components have to be taken into account in modeling process.

Using the analysis above, the loop gain Bode plots of different models are presented in Fig. 15. As can be seen, the phase of the two-frequency model at low frequencies deviates from other models as analyzed in [17]. The phase curve accuracy of the four-frequency model is improved, however, there exists an obvious deviation in magnitude. This is due to the error in calculating F_m.

It should be noted that in the four-frequency model, if the error in calculating F_m is so significant that the result is negative, then both the magnitude and phase curves will show great deviations, and the phase of the four-frequency model loop gain will start from $-270°$ instead of $-90°$ at low frequencies, as indicated in the case in Section V-A where the compensation transfer function is (66), and the corresponding F_m is -0.69 and 0.16 for the four-frequency model and the proposed model, respectively.

Another contribution of the proposed model compared to the two-frequency model and the four-frequency model lies in the simple control block diagram. In the control block diagrams of the two-frequency and the four-frequency models given in [15] and [17], any two sideband components are coupled together, which leads to many additional loops and is therefore hard to be extended to cover more frequencies. If n sideband components are incorporated besides the perturbation frequency, the total number of loops will be $(n+1)(n+2)/2$. The numerous loops make it less ready to see the physical meaning. However, in the extended-frequency-range model, the sideband components are decoupled based on (22). When considering n sideband components, the total number of loops will be $n+1$, as shown in Fig. 5, which is much simpler and offers clearer physical insight.

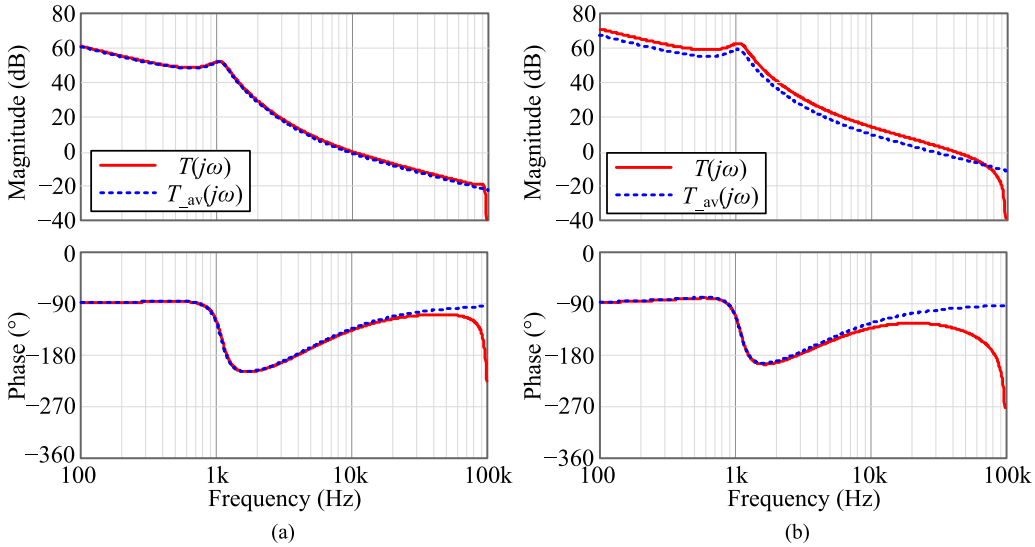

Fig. 12. Bode diagrams of $T(j\omega)$, $T_{av}(j\omega)$ with (a) controller is $G_{v\_bu1}(j\omega)$ and (b) controller $G_{v\_bu2}(j\omega)$.

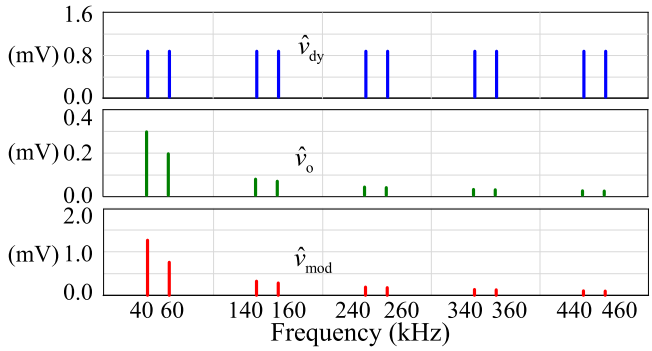

Fig. 13. Spectra of the sideband components in v_{dy}, v_o, and v_{mod} after imposing 1 mV, 40 kHz sinusoidal perturbation into v_{mod}.

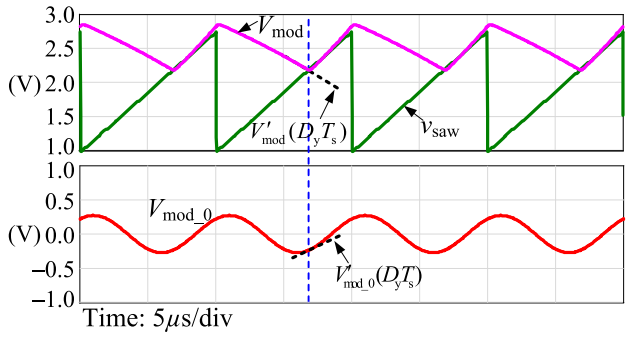

Fig. 14. Waveforms of V_{mod} and $V_{\text{mod\_0}}$ of the buck converter with G_{v_bu2} as the controller.

V. Experimental Verification

To verify the effectiveness of the proposed extended-frequency-range small-signal model, experimental measurements are taken for a buck converter and a boost converter.

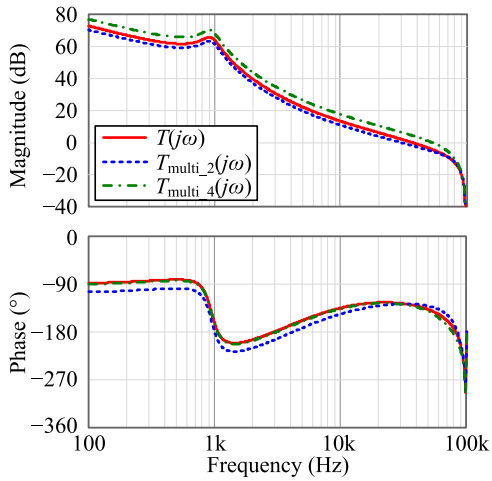

Fig. 15. Bode diagrams of the loop gains calculated by different models with compensation transfer function $G_{v\_bu2}(s)$.

A. Experimental Results of the Buck Converter

Fig. 16 gives the experimental steady-state waveforms of the buck converter with compensation transfer functions $G_{v\_bu1}(j\omega)$ and $G_{v\_bu2}(j\omega)$. The switching ripple of the modulation signal in the wideband control case is much larger than the narrowband control case. The calculated (from the model) and measured Bode diagrams of $T(j\omega)$ with controllers $G_{v\_bu1}(j\omega)$ and $G_{v\_bu2}(j\omega)$ are given in Fig. 17. The close resemblance of the calculated and measured results verifies the validity of the extended-frequency model.

To compare the stability information provided by different models, the loop gains, under the same compensation transfer function as given in the following equation, are compared for the averaged model, the two-frequency model, the four-frequency model, and our extended-frequency model:

$$G_{v\_bu3}(j\omega) = 220 + \frac{2210000}{j\omega}. \tag{66}$$

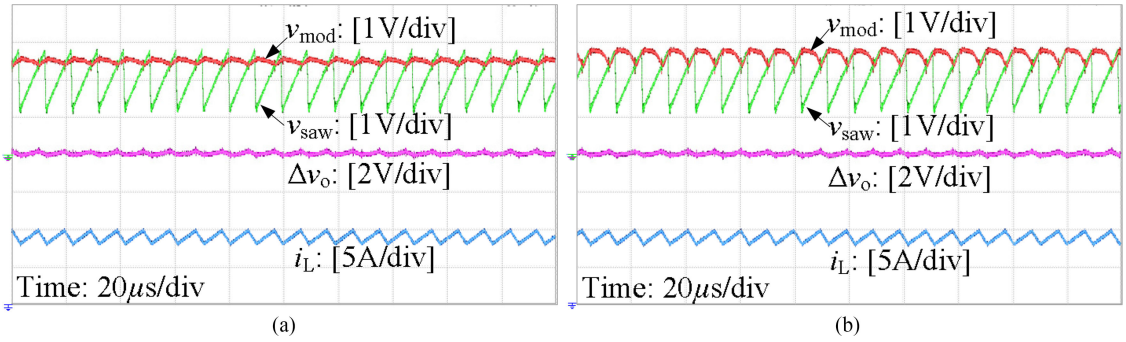

Fig. 16. Experimental waveforms of the buck converter with (a) $G_{v\_bu1}(s)$ and (b) $G_{v\_bu2}(s)$ as the controller.

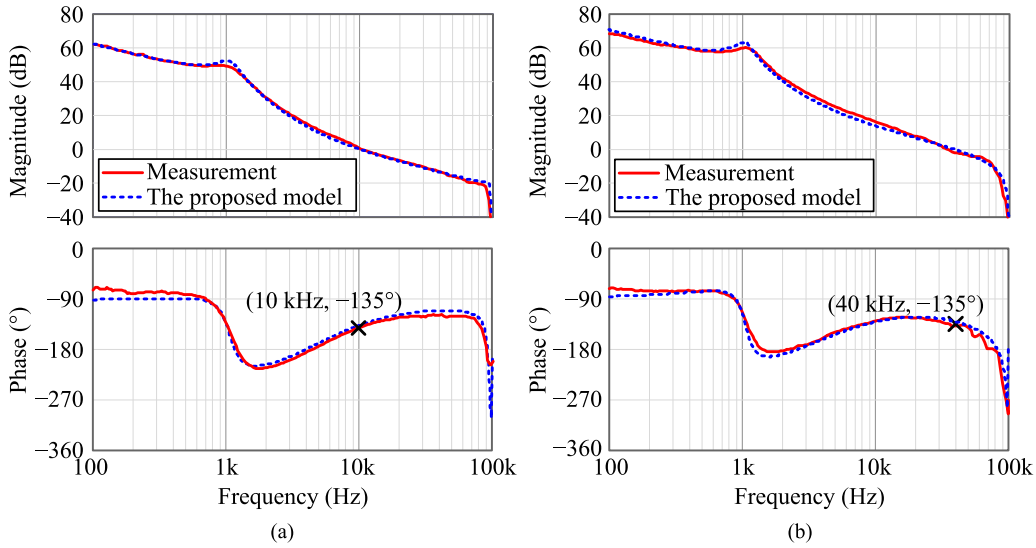

Fig. 17. Bode diagrams of the loop gain from extended-frequency model and measured result of the buck converters with (a) $G_{v\_bu1}(s)$ and (b) $G_{v\_bu2}(s)$ as the controller.

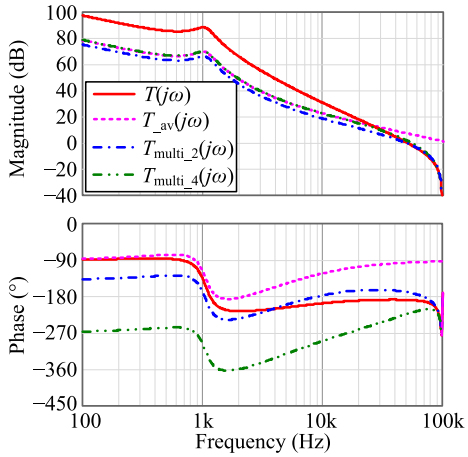

Fig. 18. Bode diagrams of the loop gains calculated by different models with $G_{v\_bu3}(s)$.

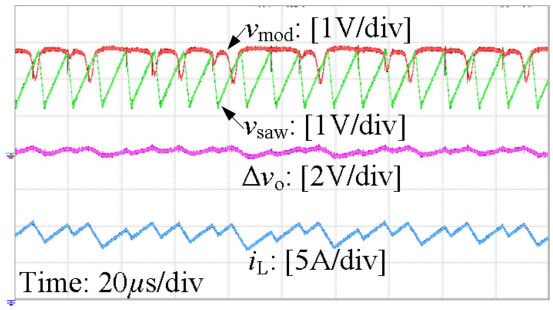

Fig. 19. Experimental waveforms of the buck converter with $G_{v\_bu3}(s)$.

The Bode diagrams of the loop gains found from the different models are plotted in Fig. 18. As seen, the phase margins provided by the averaged model, the two-frequency model, the four-frequency model, and the extended-frequency model are 90°, 14°, −45°, and −10°, respectively. Hence, the averaged and the two-frequency model both predict stable operation, whereas the four-frequency model and the extended-frequency model predict unstable operation. However, the phase of the four-frequency model starts from −270° in low frequencies due to the error in calculating F_m, and is distinct from other models. In Fig. 19, the experimental waveforms of the converter with $G_{v\_bu3}(j\omega)$ are presented, which show unstable operation, veri-

TABLE II
PARAMETERS OF THE BOOST CONVERTER

Parameter	Symbol	Value	Parameter	Symbol	Value
Input voltage	V_{in}	36 V	Output capacitor	C	300 μF
Output voltage	V_o	80 V	Capacitor ESR	R_c	0.1 Ω
Output power	P_o	500 W	Peak to peak value	V_m	1.75 V
Switching frequency	f_s	100 kHz	Voltage feedback factor	H_v	0.05
Inductor	L	95 μH			

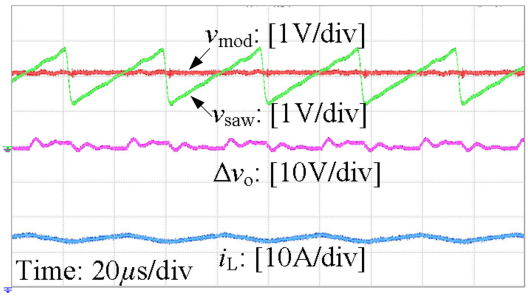

Fig. 20. Experimental waveforms of the boost converter with $G_{v\_bst}(s)$.

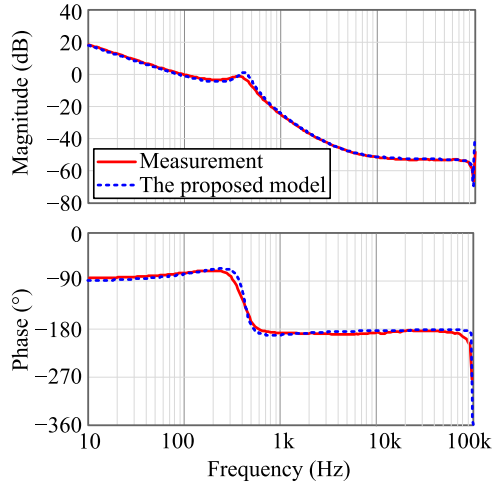

Fig. 21. Bode diagrams from extended-frequency model and measured results of the boost converter.

fying the credibility of the extended-frequency model in offering stability information.

B. Experimental Results of the Boost Converter

Table II gives the main circuit parameters of the boost converters.

The compensation transfer function of the boost converter is

$$G_{v\_bst}(s) = \frac{100}{s} + 0.05. \tag{67}$$

Fig. 20 gives the experimental results of the boost converter with compensation transfer function $G_{v\_bst}(j\omega)$. The calculated and measured Bode diagrams of loop gain $T(j\omega)$ are given in Fig. 21. The close resemblance of the calculated and measured results verifies the validity of the model. In Fig. 20, since the cutoff frequency of the boost converter is constrained by the inherent right-half-zero in the duty-cycle-to-output-voltage transfer function, the ripple modulation signal is not as large as buck converter's. However, the sideband effect and the aliasing effect can still be seen from the shape change around the switching frequency in Fig. 21.

VI. CONCLUSION

When sideband and aliasing effects of PWM are taken into consideration in modeling closed-loop dc–dc converters, a small-signal model with extended frequency range can be obtained. This model gives precise loop gain expressions and modulator gain expressions under large-ripple conditions, and hence offers accurate stability information under practical conditions. These precise expressions are, however, inconvenient to use in practical closed-loop controller design. Appropriate simplification results in an approximate expression of the loop gain, which also permits convenient and more intuitive interpretations of the sideband components and large modulation signal. Moreover, based on the extended- frequency-range model, a simple design method can be derived for effective closed-loop design of controllers for dc–dc converters.

REFERENCES

[1] R. Tymerski, V. Vorperian, F. C. Lee, and W. T. Baumann, "Nonlinear modeling of the PWM switch," *IEEE Trans. Power Electron.*, vol. 4, no. 2, pp. 225–233, Apr. 1989.
[2] R. D. Middlebrook, "Small-signal modeling of pulse-width modulated switched-mode power converter," *Proc. IEEE*, vol. 76, no. 4, pp. 343–354, Apr. 1988.
[3] G. W. Wester and R. D. Middlebrook, "Low-frequency characterization of switched DC-DC converters," *IEEE Trans. Aerosp. Electron. Syst.*, vol. AES-9, no. 3, pp. 376–385, May 1973.
[4] R. D. Middlebrook and S. Cuk, "A general unified approach to modeling switching converter power stages," in *Proc. IEEE Power Electron. Spec. Conf.*, 1976, pp. 18–34.
[5] V. Vorperian, "Simplified analysis of PWM converter using model of PWM switch, Part 1: Continuous conduction mode," *IEEE Trans. Aerosp. Electron. Syst.*, vol. AES-26, no. 3, pp. 490–496, May 1990.
[6] R. D. Middlebrook, "Predicting modulator phase lag in PWM converter feedback loops," in *Proc. IEEE Adv. Switchedmode Power Convers.*, 1981, pp. 245–250.
[7] J. Groves, "Small-signal analysis using harmonic balance methods," in *Proc. IEEE Power Electron. Spec. Conf.*, 1991, pp. 74–79.
[8] U. Vargas and A. Ramirez, "Reformulating extended harmonic domain models for accurate representation of harmonics dynamics," *IEEE Trans. Power Del.*, vol. 31, no. 6, pp. 2562–2564, Dec. 2016.
[9] M. S. Hwang and A. R. Wood, "Harmonic state-space modelling of an HVDC converter," in *Proc. IEEE 15th Int. Conf. Harmonics Quality Power*, 2012, pp. 573–580.
[10] X. Wang, F. Blaabjerg, and W. Wu, "Modeling and analysis of harmonic stability in an AC power-electronics-based power system," *IEEE Trans. Power Electron.*, vol. 29, no. 12, pp. 6421–6432, Dec. 2014.
[11] Y. Wang *et al.*, "Multiharmonic small-signal modeling of low-power PWM DC-DC converters," *ACM Trans. Des. Autom. Electron. Syst.*, vol. 22, no. 4, pp. 68–83, Jun. 2017.
[12] Y. Wang, D. Gao, D. Tannir, and P. Li, "Multi-harmonic nonlinear modeling of low-power PWM DC-DC converters operating in CCM and DCM," in *Proc. Eur. Conf. Des. Autom. Test*, 2016, pp. 409–414.
[13] S. R. Bowes and B. M. Bird, "Novel approach to the analysis and synthesis of modulation processes in power converters," in *Proc. IEE*, 1975, pp. 507–513.
[14] A. R. Brown and R. D. Middlebrook, "Sampled-data modeling of switching regulators," in *Proc. IEEE Power Electron. Spec. Conf.*, 1981, pp. 349–369.

[15] Y. Qiu, M. Xu, K. Yao, J. J. Sun, and F. C. Lee, "Multifrequency small-signal model for buck and multiphase interleaving buck converters," *IEEE Trans. Power Electron.*, vol. 21, no. 5, pp. 1185–1192, Sep. 2006.
[16] Y. Qiu, M. Xu, K. Yao, J. J. Sun, and F. C. Lee, "A generic high frequency model for the nonlinearities in buck converters," *IEEE Trans. Power Electron.*, vol. 22, no. 5, pp. 1970–1977, Sep. 2007.
[17] S.-F. Hsiao, D. Chen, C.-J. Chen, and H.-S. Nien, "A new multiple-frequency small-signal model for high-bandwidth computer V-core regulator applications," *IEEE Trans. Power Electron.*, vol. 31, no. 1, pp. 733–742, Jan. 2016.
[18] X. Li and X. Ruan, " A generic and accurate frequency- domain model for buck, boost and buck-boost converters," in *Proc. IEEE Energy Convers. Congr. Expo.*, 2014, pp. 3760–3766.
[19] K. Lee and H. Zou, "Comparison between ramp pulse modulation (RPM) and constant frequency modulation for the beat frequency oscillation in voltage regulators," in *Proc. IEEE Energy Convers. Congr. Expo.*, 2010, pp. 3101–3106.
[20] T. Qian, " Subharmonic analysis for buck converters with constant on-time control and ramp compensation," *IEEE Trans. Power Electron.*, vol. 60, no. 1, pp. 1780–1786, May 2013.
[21] A. V. Oppenheim and R. W. Schafer, *Discrete-Time Signal Processing*, 3rd ed. London, U.K.: Pearson Education, 2009.
[22] R. Tymerski, "Frequency analysis of time-interval -modulated switched networks," *IEEE Trans. Power Electron.*, vol. 6, no. 2, pp. 287–295, Apr. 1991.
[23] L. Wang and Y. Sheng, "Fast bilateral filtering using the Padé approximation," *Electron. Lett.*, vol. 53, no. 6, pp. 395–397, Mar. 2017.
[24] R. B. Ridley, "A new continuous-time model for current-mode control," *IEEE Trans. Power Electron.*, vol. 6, no. 2, pp. 271–280, Apr. 1991.

Xin Li received the B. S. degree in electrical engineering and automation in 2012 from the Nanjing University of Aeronautics and Astronautics, Nanjing, China, where he is currently working toward the Ph.D. degree in electrical engineering.

His current research interests include modeling and control of dc–dc converters and cascaded power systems.

Xinbo Ruan (M'97–SM'02–F'16) received the B.S. and Ph.D. degrees in electrical engineering from the Nanjing University of Aeronautics and Astronautics (NUAA), Nanjing, China, in 1991 and 1996, respectively.

In 1996, he joined the Faculty of Electrical Engineering Teaching and Research Division, NUAA, where he became a Professor with the College of Automation Engineering in 2002, and has been engaged in teaching and research in the field of power electronics. From August to October 2007, he was a Research Fellow with the Department of Electronic and Information Engineering, Hong Kong Polytechnic University, Hong Kong, China. Since March 2008, he has been with the School of Electrical and Electronic Engineering, Huazhong University of Science and Technology, Wuhan, China. He is a Guest Professor with Beijing Jiaotong University, Beijing, China, with Hefei University of Technology, Hefei, China, and also with Wuhan University, Wuhan. He has authored or coauthored nine books and more than 200 technical papers published in journals and conferences. His main research interests include soft-switching dc–dc converters, soft-switching inverters, power factor correction converters, modeling converters, power electronics systems integration, and renewable energy generation systems.

Prof. Ruan was the recipient of the Delta Scholarship by the Delta Environment and Education Fund in 2003 and was the recipient of the Special Appointed Professor of the Chang Jiang Scholars Program by the Ministry of Education, China in 2007. From 2005 to 2013, he served as the Vice President of the China Power Supply Society, and since 2008, he has been a member of the Technical Committee on Renewable Energy Systems within the IEEE Industrial Electronics Society. He is currently working as an Associate Editor for the IEEE TRANSACTIONS ON INDUSTRIAL ELECTRONICS, the IEEE TRANSACTIONS ON POWER ELECTRONICS, the IEEE JOURNAL OF EMERGING AND SELECTED TOPICS ON POWER ELECTRONICS, and the IEEE TRANSACTIONS ON CIRCUITS AND SYSTEMS-II. He is an IEEE Fellow.

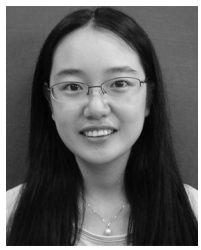

Qian Jin (S'14) received the B.S. and Ph.D. degrees in electrical engineering and automation from the Nanjing University of Aeronautics and Astronautics, Nanjing, China, in 2011 and 2017, respectively.

Her current research interests include envelope tracking power supplies and dc–dc converters.

Mengke Sha received the B.S. degree in electrical engineering in 2015 from the Nanjing University of Aeronautics and Astronautics, Nanjing, China, where he is currently working toward the M.S. degree in electrical engineering.

His main research interests include modeling and control of dc–dc converters.

Chi K. Tse (M'90–SM'97–F'06) received the B.Eng. (first class Hons.) and Ph.D. degrees in electrical engineering from the University of Melbourne, Parkville, VIC, Australia, in 1987 and 1991, respectively.

He is currently a Chair Professor at the Hong Kong Polytechnic University, Hong Kong, China, where he was the Head of the Department of Electronic and Information Engineering from 2005 to 2012.

Dr. Tse is the recipient of a number of research and industry awards, including Prize Paper Awards by the IEEE TRANSACTIONS ON POWER ELECTRONICS in 2001 and 2015, *RISP Journal of Signal Processing* Best paper Award in 2014, Best paper Award by the *International Journal of Circuit Theory and Applications* in 2003, two Gold Medals at the International Inventions Exhibition in Geneva in 2009 and 2013, a Silver Medal at the International Invention Innovation Competition in Canada in 2016. He has been recognized by the academic and research communities, receiving honorary professorships at several Chinese and Australian universities, the Chang Jiang Scholar Chair Professorship, the IEEE Distinguished Lectureship, the Distinguished Research Fellowship by the University of Calgary, and the Gledden Fellowship and International Distinguished Professorship-at-Large by the University of Western Australia. While with the Hong Kong Polytechnic University, he was the recipient of President's Award for Outstanding Research Performance twice, the Faculty Research Grant Achievement Award twice, the Faculty Best Researcher Award, and several teaching awards. He serves and has served as the Editor-in-Chief for the IEEE TRANSACTIONS ON CIRCUITS AND SYSTEMS II (2016–2019), IEEE CIRCUITS AND SYSTEMS MAGAZINE (2012–2015), Editor-in-Chief for the IEEE CIRCUITS AND SYSTEMS SOCIETY NEWSLETTER (since 2007), Associate Editor for three IEEE Journal/Transactions, Editor for the *International Journal of Circuit Theory and Applications*, and is on the editorial boards of a few other journals. He also serves as member of several government committees and panels.